Single-site iron-anchored amyloid hydrogels as catalytic platforms for alcohol detoxification

Jiaqi Su [1,2,9] ✉, Pengjie Wang [3,9], Wei Zhou[4], Mohammad Peydayesh [1], Jiangtao Zhou [1], Tonghui Jin[1], Felix Donat [5], Cuiyuan Jin[6], Lu Xia [7], Kaiwen Wang [7], Fazheng Ren [3], Paul Van der Meeren [2], F. Pelayo García de Arquer [7] & Raffaele Mezzenga [1,8] ✉

Constructing effective antidotes to reduce global health impacts induced by alcohol prevalence is a challenging topic. Despite the positive effects observed with intravenous applications of natural enzyme complexes, their insufficient activities and complicated usage often result in the accumulation of toxic acetaldehyde, which raises important clinical concerns, highlighting the pressing need for stable oral strategies. Here we present an effective solution for alcohol detoxification by employing a biomimetic-nanozyme amyloid hydrogel as an orally administered catalytic platform. We exploit amyloid fibrils derived from β-lactoglobulin, a readily accessible milk protein that is rich in coordinable nitrogen atoms, as a nanocarrier to stabilize atomically dispersed iron (ferrous-dominated). By emulating the coordination structure of the horseradish peroxidase enzyme, the single-site iron nanozyme demonstrates the capability to selectively catalyse alcohol oxidation into acetic acid, as opposed to the more toxic acetaldehyde. Administering the gelatinous nanozyme to mice suffering from alcohol intoxication significantly reduced their blood-alcohol levels (decreased by 55.8% 300 min post-alcohol intake) without causing additional acetaldehyde build-up. Our hydrogel further demonstrates a protective effect on the liver, while simultaneously mitigating intestinal damage and dysbiosis associated with chronic alcohol consumption, introducing a promising strategy in effective alcohol detoxification.

Although widely enjoyed for its social and relaxing effects (Supplementary Fig. 1), alcohol consumption consistently poses significant risks to public health. In fact, in 2016 alone, harmful alcohol consumption resulted in nearly three million deaths and 132.6 million disability-adjusted life years[1–4]. Existing therapies, mainly relying on endogenous enzymes[5–7], offer only temporary relief from symptoms, such as nausea and headaches, but fail to address other underlying issues, such as drowsiness, exhaustion and chronic alcoholism.

Nanocomplexes with multiple complementary hepatic enzymes have emerged as an effective approach for accelerating human alcohol metabolism[8,9]. Although promising, a significant obstacle arises from the insufficient activity of commercially available enzymes, leading to the accumulation of a more hazardous intermediate, acetaldehyde, and possibly damage to human organs. Furthermore, natural enzymes possess major disadvantages, such as high cost, poor physicochemical stability and challenging storage, which have so far impeded the

A full list of affiliations appears at the end of the paper. ✉e-mail: jiaqi.su@hest.ethz.ch; raffaele.mezzenga@hest.ethz.ch
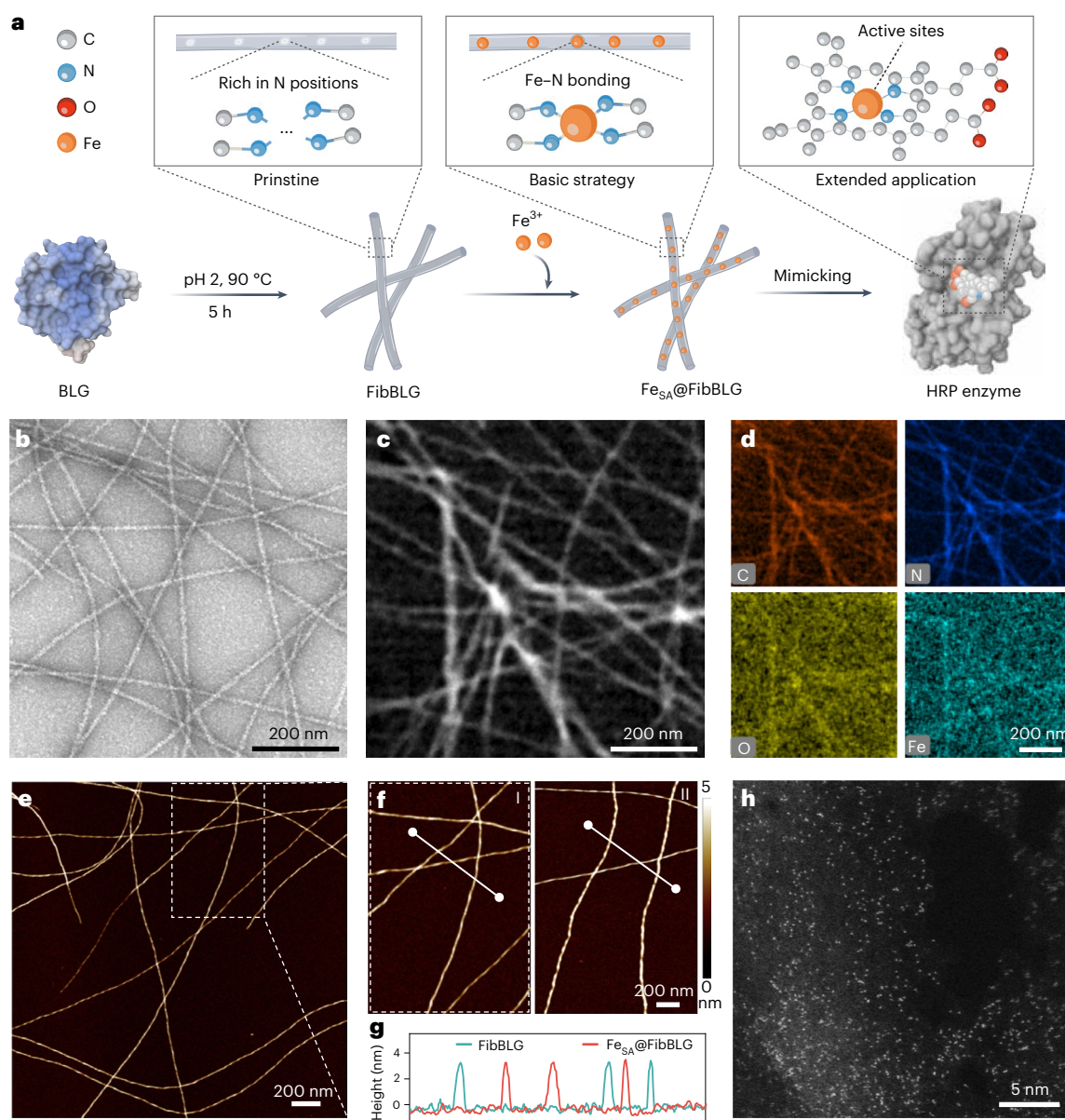
Fig. 1 | Synthesis and morphology characterization of Fe$_{SA}$@FibBLG.
a, Illustration of the synthesis process of Fe$_{SA}$@FibBLG. **b**–**d**, TEM image (**b**),
HAADF-STEM image (**c**) and the corresponding EDS mapping images (**d**) of
Fe$_{SA}$@FibBLG. **e**–**g**, AFM images of Fe$_{SA}$@FibBLG (**e**, **f (I)**) and FibBLG (**f (II)**) on
the mica surface and (**g**) the corresponding height profiles of the white auxiliary
lines. **h**, Representative HAADF-STEM image of Fe$_{SA}$@FibBLG. The images
presented in **b**–**f**,**h** are representative of six technical replicates ($n = 6$), each
yielding similar results.

practical application of these complexes for alcohol detoxification
purposes.

Over the past decades, advances in nanotechnology have facili-
tated the evolution of artificial enzymes into nanomaterials, that is,
nanozymes, which have ignited enormous scientific interest across
diverse fields, ranging from in vitro biosensing and detection to in vivo
therapeutics[10–13]. Inspired by natural enzyme frameworks, researchers
have predominantly focused on atomically distributed metal catalysts,
in which the catalytic centre of natural enzymes is replicated at the
atomic level[14–16]. These single-site catalysts, designed with well-defined
electronic and geometric architectures, possess excellent catalytic
capabilities, holding great potential as viable substitutes for natural
enzymes. Given these promising prospects, attempts have been made
to develop biomimetic nanozymes for alcohol detoxification by using,
for example, natural enzymes on exogenous supports such as graphene
oxide quantum dots or metal–organic framework nanozymes[17,18]. How-
ever, these approaches still either rely on natural enzymes or offer

indirect effects, underscoring the potential for substantial design
enhancements. The critical, yet challenging, aspect is the design of
efficient single-site catalysts that are capable of converting ethanol
into less-toxic acetic acid, or further into carbon dioxide and water,
while minimizing the generation of acetaldehyde. Additionally, the
task also lies in developing an orally administerable nanozyme that
can withstand the gastrointestinal environment and which features
no additional toxicity.

In this article, we report a biomimetic-nanozyme amyloid hydrogel
to alleviate the deleterious effects of alcohol consumption via oral
administration. Within this platform, single-site iron-anchored amyloid
fibrils, an original kind of atomic-level engineered nanozyme featur-
ing a similar coordination structure to horseradish peroxidase and
with remarkable peroxidase-like activity, are used to efficiently cata-
lyse alcohol oxidation. Specifically, the resultant nanozyme exhibits
excellent selectivity in favour of acetic acid production. The catalytic
activity of the gelatinous nanozyme could largely tolerate the digestive

process, leading to a substantial decrease in blood alcohol levels in alcoholic mice, while avoiding the additional build-up of acetaldehyde. We finally demonstrate that this hydrogel also achieves heightened liver protection and substantial alleviation of intestinal damage and dysbiosis, thereby underscoring its potential as an improved therapeutic approach for alcohol-related conditions. By employing atomic-level design and harnessing the capabilities of nanozymes, our study offers promising insights into the development of efficient and targeted alcohol antidotes, with potential benefits for both liver protection and gastrointestinal health.

Synthesis of single-site iron-anchored β-lactoglobulin fibrils

Diverging from conventional methods that use inorganic carriers, in the current work, we sought to utilize a readily available protein material, β-lactoglobulin (BLG) amyloid fibrils, as the supportive framework for atomically dispersed iron. In addition to their intrinsic binding affinity to various metal ions[19], including iron, the large aspect ratio of protein filaments (Supplementary Fig. 2a) and tacked-up β-sheet units also enhance the accessibility of potential binding sites, thereby facilitating the high-density loading of iron atoms. Moreover, BLG fibrils can be easily derived from native BLG, a readily available milk protein, and have very recently been demonstrated safe nutrition ingredients by a comprehensive in vitro and in vivo assessment[20], meeting the requirements for potential oral administration[21]. Moreover, the exceptional gelling property of BLG fibrils allows for the easy production of hydrogels[22], which anticipates a delayed digestion process and a prolonged action time within the gastrointestinal tract due to their high viscoelasticity[23,24].

The single-site iron-anchored BLG fibrils (Fe$_{SA}$@FibBLG) catalyst was synthesized by a straightforward wetness impregnation procedure (Fig. 1a), which involved exposing a dispersion of BLG fibrils in a mixture of ethanol and polyethylene glycol 200 (PEG200) to a Fe(NO$_3$)$_3$ PEG200 solution. During this process, the natural occurrence of nitrogen in BLG fibrils coordinated with iron ions to form functional Fe–N–C active sites. The resulting precipitate was lyophilized and collected after multiple rounds of centrifugation and washing.

Having synthesized Fe$_{SA}$@FibBLG, we then performed a comprehensive characterization of the material using multiple analytical techniques. The morphology of Fe$_{SA}$@FibBLG, which retains a nanometre-scale diameter consistent with pure BLG fibrils (Supplementary Fig. 2b), suggests minimal structural impact from the integration of iron (Fig. 1b and Supplementary Fig. 2b). The iron was homogeneously dispersed across the BLG fibril framework, as evidenced by a significant overlap of the Fe K-edge profile with the elemental composition of the BLG fibrils (Fig. 1c,d and Supplementary Fig. 2c). Atomic force microscopy (AFM) images confirmed a consistent height of approximately 3 nm both before and after iron integration, verifying the negligible presence of crystalline iron or oxide species (Fig. 1e,f,g). As shown in Fig. 1h and Supplementary Fig. 2d–f, the presence of individual bright dots with a size below 0.2 nm clearly demonstrated the atomic dispersion of single iron atoms over Fe$_{SA}$FibBLG, indicating that iron, upon participating in the synthetic procedure described above, is present exclusively in single-site form on the BLG fibrils.

Structural analysis of Fe$_{SA}$@FibBLG

The coordination environment of iron within Fe$_{SA}$@FibBLG was elucidated by X-ray absorption fine structure (XAFS) spectroscopy[25]. Figure 2a shows that the pre-edge position for Fe$_{SA}$@FibBLG resided between the positions of iron foil (metallic iron) and Fe$_2$O$_3$. The white line area located at higher binding energy demonstrates a lower oxidation state and different coordination environments compared with Fe$_2$O$_3$ (ref. 26). X-ray absorption near-edge spectroscopy (XANES) features are valuable for discerning site symmetry around iron in macromolecular complexes[27]. A distinct prominent pre-edge feature below 7,120 eV indicates the ferrous iron (Fe^{2+}) square-planar coordination in

iron(II) phthalocyanine (FePc), whereas in Fe$_{SA}$@FibBLG this feature is slightly reduced due to deviations from ideal square-planarity[28]. The XANES spectrum of Fe$_{SA}$@FibBLG (Fig. 2a, inset) closely resembles that of FePc, implying a positively charged ionic state of iron within Fe$_{SA}$@FibBLG (Fe$^{\delta+}$, where the average δ is close to 2). Further insights were obtained from extended X-ray absorption fine structure (EXAFS) spectra in R-space (Fig. 2b), which revealed a single peak at approximately 1.4 Å. From comparison with reference materials this peak was attributable to the backscattering between iron and lighter atoms, primarily nitrogen (Fig. 2b), supporting the atomic dispersion of iron sites within Fe$_{SA}$@FibBLG. Wavelet transform analysis differentiated the sample from the iron foil reference by showing a single maximum intensity at approximately 4 Å^{-1} and 1.4 Å, suggesting significant Fe–N contributions (Fig. 2c and Supplementary Fig. 3), with the coordination number of iron estimated to be 4.5 (Fig. 2d and Supplementary Table 1). However, given the challenge in distinguishing Fe–N from Fe–O coordination compared to references such as FePc and Fe$_2$O$_3$, it is crucial to emphasize the potential existence of Fe–O bonds. Collectively, these findings confirmed that iron in Fe$_{SA}$@FibBLG exists as single-site iron, devoid of any crystalline or oxide iron metal structure and mainly coordinates with nitrogen atoms. X-ray photoelectron spectroscopy (XPS) analysis of Fe$_{SA}$@FibBLG further identified distinct binding states of carbon, nitrogen, oxygen and iron, demonstrating a majority of single-site iron in the Fe^{2+} state and the existence of Fe–N coordination (Supplementary Figs. 4 and 5)[29–31].

Next, we performed a density functional theory (DFT) calculation for the process of anchoring a ferric ion onto the BLG fibril structure. Since the formation of BLG fibrils involved the participation of multiple peptides assembling in a random manner, here a model nanofibre structure was generated in silico based on repetitive amyloid-forming fragments (LACQCL) from BLG, using an all-atom molecular dynamics (AAMD) simulation (Fig. 2e)[19]. An evident periodic nanofibril was formed at 10 ns containing 102 repetitive fragments, where a peptide dimer with verified thermodynamic stability was intercepted for DFT calculation (Supplementary Fig. 6). As shown in Fig. 2f, the blue isosurface observed between the iron atom and surrounding nitrogen atoms corresponds to strong attractive interactions between iron and nitrogen, potentially arising from the sharing of electron pairs between the iron and nitrogen atoms (Supplementary Fig. 7). This was further verified by the existence of the prominent peak at approximately −0.03 in the scatter plot (Fig. 2f). These results clearly demonstrate that the BLG fibrils possessed effective binding sites that were capable of capturing iron atoms through Fe–N coordination, enabling the formation of active iron centres in Fe$_{SA}$@FibBLG.

Peroxidase-like activity of Fe$_{SA}$@FibBLG

The coordination structure of the catalytic sites in our Fe$_{SA}$@FibBLG was similar to that of the horseradish peroxidase enzyme (Supplementary Fig. 8a)[32]. Inspired by this similarity, we characterized the peroxidase-like activities of Fe$_{SA}$@FibBLG by studying the facilitated chromogenic reactions through catalysing artificial substrates of peroxidase (for example, 3,3′,5,5′-tetramethylbenzidine (TMB), 2,2′-azino-bis(3-ethylbenzothiazoline-6-sulfonic acid) or o-phenylenediamine) in the presence of H$_2$O$_2$ (Supplementary Fig. 8b). By using the general method described in the current work, two comparison catalysts, namely, single-site iron-anchored BLG (Fe$_{SA}$@BLG), and iron-nanoparticle-anchored BLG fibrils (FeNP@FibBLG), were synthesized and then used to characterize the enzymatic activity (Supplementary Figs. 9 and 10 and Supplementary Table 2). Using TMB as a substrate, the specific activity (SA) values (U mg^{-1}) of these nanozymes were measured: the SA of Fe$_{SA}$@FibBLG was markedly superior, at 95.0 U mg^{-1}, approximately 1.7 and 10.1 times higher than the SAs of Fe$_{SA}$@BLG (57.3 U mg^{-1}) and FeNP@FibBLG (9.38 U mg^{-1}), respectively (Fig. 3a). Steady-state kinetic assays revealed that Fe$_{SA}$@FibBLG exhibited superior catalytic performance among the

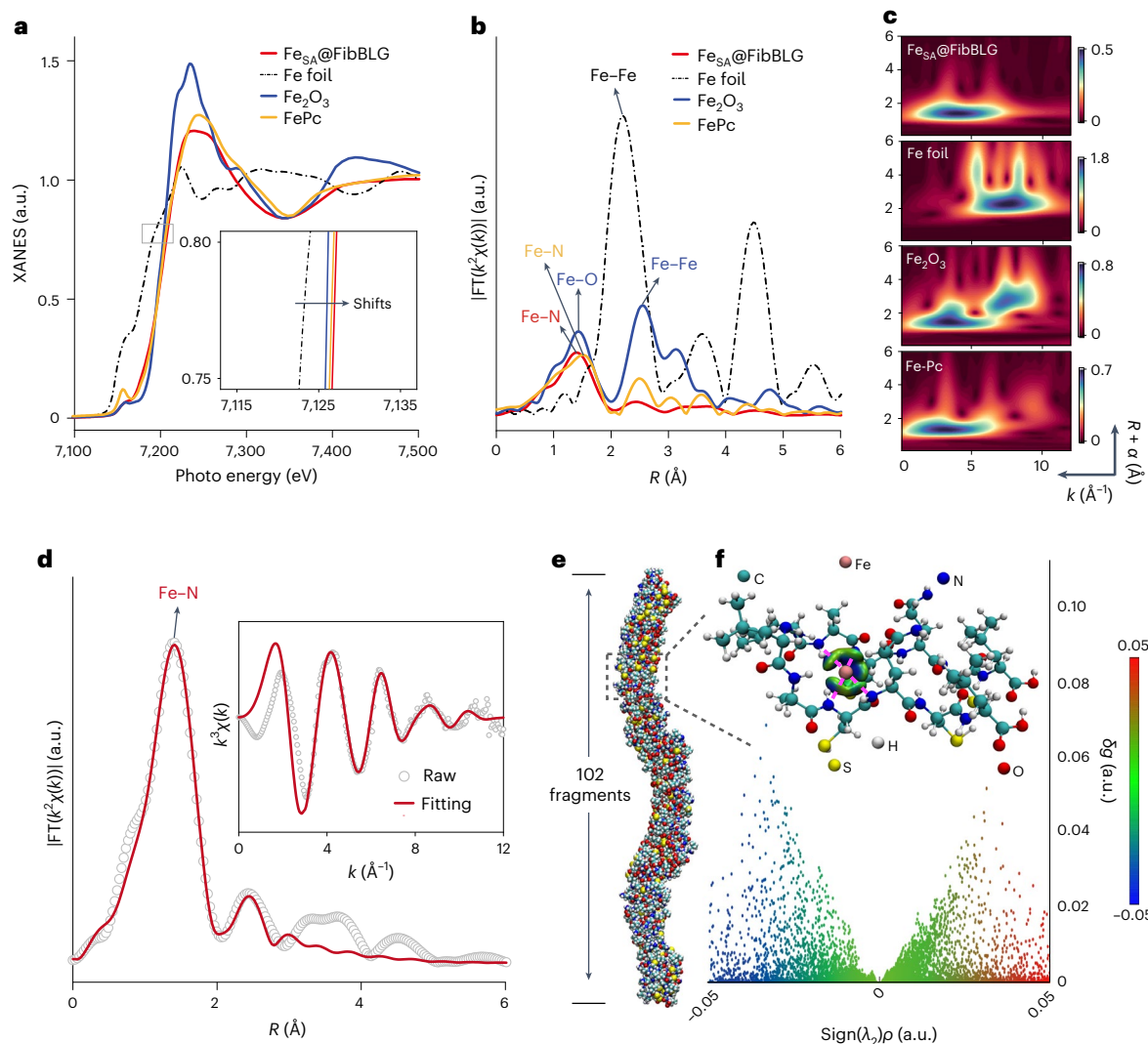**Fig. 2 | Atomic structure characterization of Fe$_{SA}$@FibBLG. a**, Normalized XANES spectra at the Fe K-edge of Fe$_{SA}$@FibBLG along with reference samples. **b**, Fourier-transformed (FT) magnitudes of the experimental Fe K-edge EXAFS signals of Fe$_{SA}$@FibBLG along with reference samples. **c**, Wavelet transform analysis of Fe K-edge EXAFS data. **d**, Fitting curves of the EXAFS of $_{FeSA@FibBLG}$ in the *R*-space and *k*-space (inset). Fitting results are summarized in Supplementary Table 1. **e**, Representative snapshots of the assembly structure of 102 amyloid-forming fragments (LACQCL) from BLG in the process of AAMD simulation using the

Gromacs54A force field at 10 ns. **f**, The 3D gradient isosurfaces and corresponding 2D scatter diagram of δg versus sign(λ$_2$)ρ for possible non-covalent interactions between a single iron atom and dimer intercepted from BLG fibril segments in **e** through DFT simulation. δg is a quantitative measure derived from comparing electron density gradients in the presence and absence of interference, highlighting the penetration of electron density from one Bader atom to its neighbor; sign(λ$_2$)ρ is a scalar field value used to describe the product of the sign of the second eigenvalue (λ$_2$) of the Hessian matrix of a scalar field and the scalar field's density (ρ).

tested nanozymes in oxidizing TMB, with remarkable kinetic parameters including maximum reaction rate (V_{max} = 0.788 μM s^{-1}), turnover number (K_{cat} = 21.9 min^{-1}), catalytic efficiency (K_{cat}/K_m = 5.47 × 10^8 M^{-1} min^{-1}) and selectivity (K_m = 4.00 × 10^{-2} mM) (Fig. 3b and Supplementary Table 3). We also determined the kinetic parameters for the H$_2$O$_2$ substrate, which further substantiated the exceptional catalytic performance of Fe$_{SA}$@FibBLG (Supplementary Table 4).

Interestingly, Fe$_{SA}$@FibBLG also exhibited a notable capacity for catalytically oxidizing ethanol and acetaldehyde in the presence of H$_2$O$_2$ (Fig. 3c–f). The SA of Fe$_{SA}$@FibBLG achieved a value of 7.90 U mg^{-1} when ethanol was used as the substrate, remarkably surpassing the other two reference catalysts. The superior catalytic efficacy of Fe$_{SA}$@FibBLG with respect to ethanol was further confirmed by determining its kinetic parameters, which indicate it achieves a catalytic efficiency (K_{cat}/K_m = 4.11 × 10^5 M^{-1} min^{-1}) that exceeds that of Fe$_{SA}$@BLG (K_{cat}/K_m = 8.66 × 10^4 M^{-1} min^{-1}) by 4.7 times and FeNP@FibBLG (K_{cat}/K_m = 9.25 × 10^3 M^{-1} min^{-1}) by 44.4 times (Supplementary Table 5). Fe$_{SA}$@FibBLG also manifested the lowest K_m value when ethanol was the substrate,

signifying its excellent affinity towards ethanol. It is important to note that Fe$_{SA}$@FibBLG could directly oxidize ethanol to acetic acid, yielding formic acid as the only by-product, without generating any detectable acetaldehyde intermediate, as evidenced by ^{1}H NMR (Fig. 3d, inset).

To explain this, we performed a steady-state kinetic analysis of Fe$_{SA}$@FibBLG participating in acetaldehyde oxidation. We found Fe$_{SA}$@FibBLG to have the lowest K_m value of the evaluated nanozymes, signifying its superior substrate affinity towards acetaldehyde. The K_{cat}/K_m for this reaction (3.89 × 10^5 M^{-1} min^{-1}) was very close to that for ethanol oxidation (4.11 × 10^5 M^{-1} min^{-1}) (Supplementary Tables 5 and 6). Upon the reaction between these nanozymes and H$_2$O$_2$, the electron paramagnetic resonance (EPR) spectrum exhibited characteristic peaks associated with 5,5-dimethyl-pyrroline-*N*-oxide–OH·, with Fe$_{SA}$@FibBLG displaying the strongest EPR signal, indicating the highest production of OH· (Fig. 3g). The same characteristic peaks were observed in the EPR spectrum of the Fe$_{SA}$@FibBLG/H$_2$O$_2$/ethanol reaction system (Supplementary Fig. 17), confirming the existence of OH· in ethanol oxidation—a finding that agrees with numerous studies demonstrating
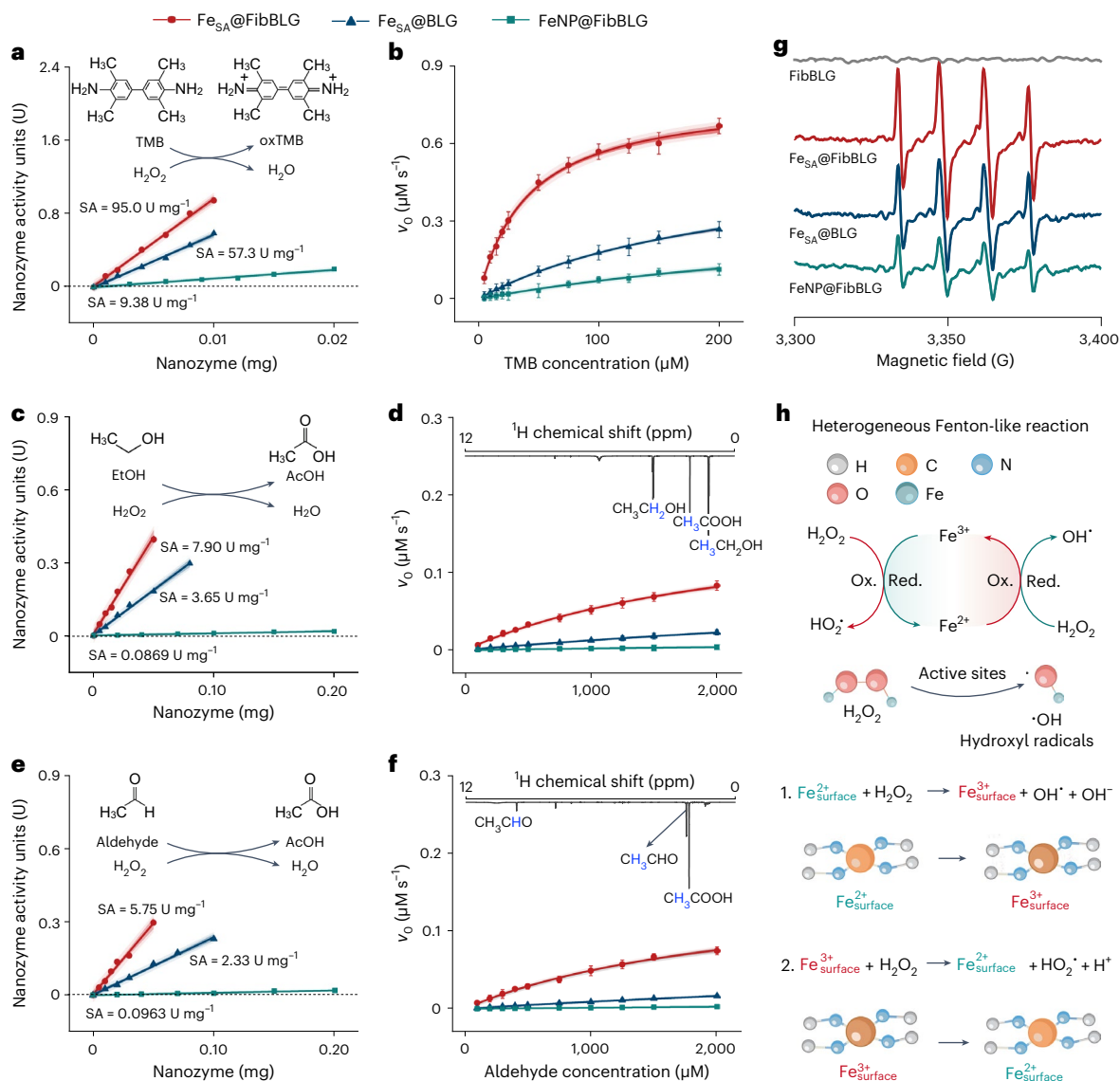
Fig. 3 | Peroxidase-like activity of single-site iron-anchored BLG fibrils.
a–**f**, Typical Michaelis–Menten curves of Fe_{SA}@FibBLG, Fe_{SA}@BLG and FeNP@FibBLG by varying the TMB (**a**), ethanol (**c**) and acetaldehyde (**e**) concentrations in the presence of H_2O_2. Comparison of the SAs (U mg^{-1}) of Fe_{SA}@FibBLG, Fe_{SA}@BLG and FeNP@FibBLG on TMB (**b**), ethanol (**d**) and acetaldehyde (**f**) oxidation in the presence of H_2O_2. One nanozyme activity unit (U) is defined as the amount of nanozyme that catalyses 1 µmol of product per minute.

The SAs (U mg^{-1}) were determined by plotting the nanozyme activities against their weight and measuring the gradients of the fitting curves. ^{1}H NMR spectrum of the reaction products of Fe_{SA}@FibBLG-catalysed ethanol (inset **d**) and acetaldehyde (inset **f**) oxidation. Data are presented as the mean ± s.d. from $n = 3$ independent experiments. **g**, EPR spectra of 5,5-dimethyl-pyrroline-N-oxide/ H_2O_2 solution upon the addition of nanozymes. **h**, Schematic illustration of the peroxidase-like activities of Fe_{SA}@FibBLG when exposed to various substrates.

the efficacy of OH$^.$ in oxidizing diverse organic compounds, including ethanol and acetaldehyde[33,34]. Nevertheless, it is essential to emphasize that our investigation serves as a preliminary exploration of the free radicals involved in this reaction; a more comprehensive mechanistic investigation is required for an in-depth understanding of the catalytic process.

Additionally, the catalytic stability of Fe_{SA}@FibBLG was assessed by high-resolution transmission electron microscopy (TEM), high-angle annular dark-field scanning transmission electron microscopy (HAADF-STEM), energy-dispersive spectroscopy elemental analysis, X-ray diffraction and XPS (Supplementary Figs. 18 and 19). Fe_{SA}@FibBLG did not exhibit substantial morphological or oxidation state alterations and effectively preserved the high atomic dispersion of iron active sites throughout the catalysis. It is also worth mentioning that Fe_{SA}@FibBLG retained at least 95.2% and 84.1% of its activity after undergoing 3 h of digestion in simulated gastric and intestinal fluids, respectively

(Supplementary Fig. 20). The robust stability observed in Fe_{SA}@FibBLG may be due to the reduction effects of BLG fibril support[21].

Protective potential on acute alcohol intoxication

Even a single new onset of blood alcohol that exceeds the detoxifying capability of the hepatic system can induce individual symptoms of acute alcohol intoxication, such as hepatocyte destruction, stress response and cognitive deficits[35,36]. To mitigate potential damage to the human digestive tract from direct H_2O_2 ingestion, a biomimetic cascade catalysis system was designed by integrating gold nanoparticles (AuNPs) for onsite and sustainable H_2O_2 generation[37–39]. AuNPs have demonstrated exceptionally efficient and enduring catalytic activity similar to glucose oxidase, which allows the conversion of glucose into gluconic acid, accompanied by the production of adequate H_2O_2 (Supplementary Fig. 21). Because protein fibrils transiently remained
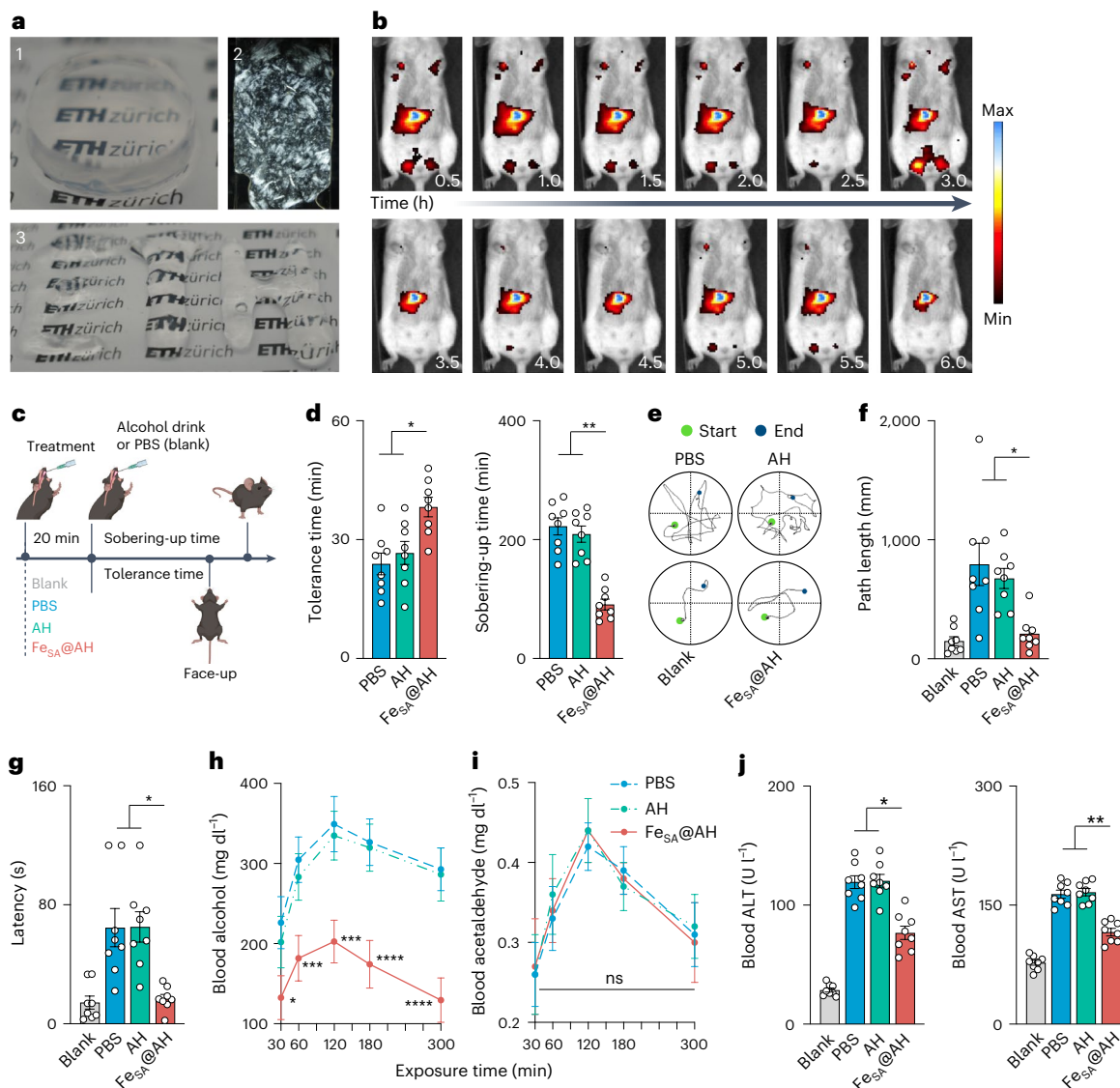
Fig. 4 | Effect of Fe$_{SA}$@AH as a prophylactic for acute alcohol intoxication.
a, Visualization (1) and microstructures (2) of Fe$_{SA}$@AH under polarized light, and injectability test (3). **b**, Time-series images of gastrointestinal translocation of [^{18}F]FDG-loaded Fe$_{SA}$@AH in mice (0–6 h). **c**, Schematic of acute alcohol intoxication model construction (Methods). Created with BioRender.com. **d**, Effect of different treatment (PBS, AH and Fe$_{SA}$@AH) on alcohol tolerance time and sobering-up time in C57BL/6 mice. **e**, Representative trajectory of search strategies of mice with different treatments. **f**,**g**, Escape latencies (**f**) and path length (**g**) of four groups of mice. **h**,**i**, Mean concentrations of blood alcohol (**h**) and acetaldehyde (**i**) in alcohol-intoxicated mice treated with PBS, AH and Fe$_{SA}$@AH. **j**, Serum levels of ALT and AST enzyme levels in four groups of mice. Data are obtained for $n = 8$ independent biological replicates, mean ± s.e.m. P values in **d**,**f**,**g**,**h**,**j** were tested by one-way analysis of variance followed by Tukey–Kramer test. *$P < 0.05$, **$P < 0.01$, ***$P < 0.001$, ****$P < 0.0001$.

and were mostly digested (generally within 4 h) in the gastrointestinal tract[20], where the majority of alcohol was absorbed, a salt-induced technique[40] (Methods) was followed to fabricate the AuNP-attached Fe$_{SA}$@FibBLG amyloid hydrogel (Fe$_{SA}$@AH) (Supplementary Fig. 22) to achieve prolonged retention within the gastrointestinal tract, and, thereby, an enhanced overall capacity for ethanol oxidation. The resultant Fe$_{SA}$@AH showed typical self-standing ability, obvious nanofibril structures (exceptional birefringence under polarized light) and good syringability (Fig. 4a). We then labelled Fe$_{SA}$@AH with [^{18}F] fluoro-2-deoxyglucose ([^{18}F]FDG) and visualized its transportation in C57BL/6 mice by using micro positron emission tomography (PET)–computed tomography (CT) scanning. The metabolism of Fe$_{SA}$@AH took more than 6 h in the upper gastrointestinal tract after gavage, which indicated an extended retention time in vivo due to the hydrogel nature of the compound[20].

The prophylactic benefits of Fe$_{SA}$@AH administration were assessed in an alcohol-treated murine model[41] (Fig. 4c). A group of ethanol-free, but

PBS-gavaged mice served as a negative control; all the ethanol-gavaged mice were asleep for alcohol intoxication. Although they tolerated alcohol intake for a longer period of time (~40 min), the Fe$_{SA}$@AH mice were awoken significantly earlier (~2 h) than other intoxicated groups (Fig. 4d). We then conducted the Morris water maze (MWM) test 6 h post-alcohol intake to quantitatively assess murine spatial reference memory (Fig. 4e). Grouped mean swimming speeds of alcohol-exposed mice were comparable to those of the blank group, indicating recovery of fundamental activities (Supplementary Fig. 25a). However, PBS- and AH-treated mice showed increased search time and distance to locate the hidden platform, whereas the mice given Fe$_{SA}$@AH demonstrated markedly improved navigational efficiency (Fig. 4f,g). Additionally, distinct search strategies were observed, with PBS and AH groups favouring less efficient patterns, in contrast to the strategic approaches of the Fe$_{SA}$@AH and control groups (Supplementary Fig. 25b).

Aetiologically, behavioural abnormalities were attributed to alcohol and its in vivo intermediate metabolite, acetaldehyde[42], and
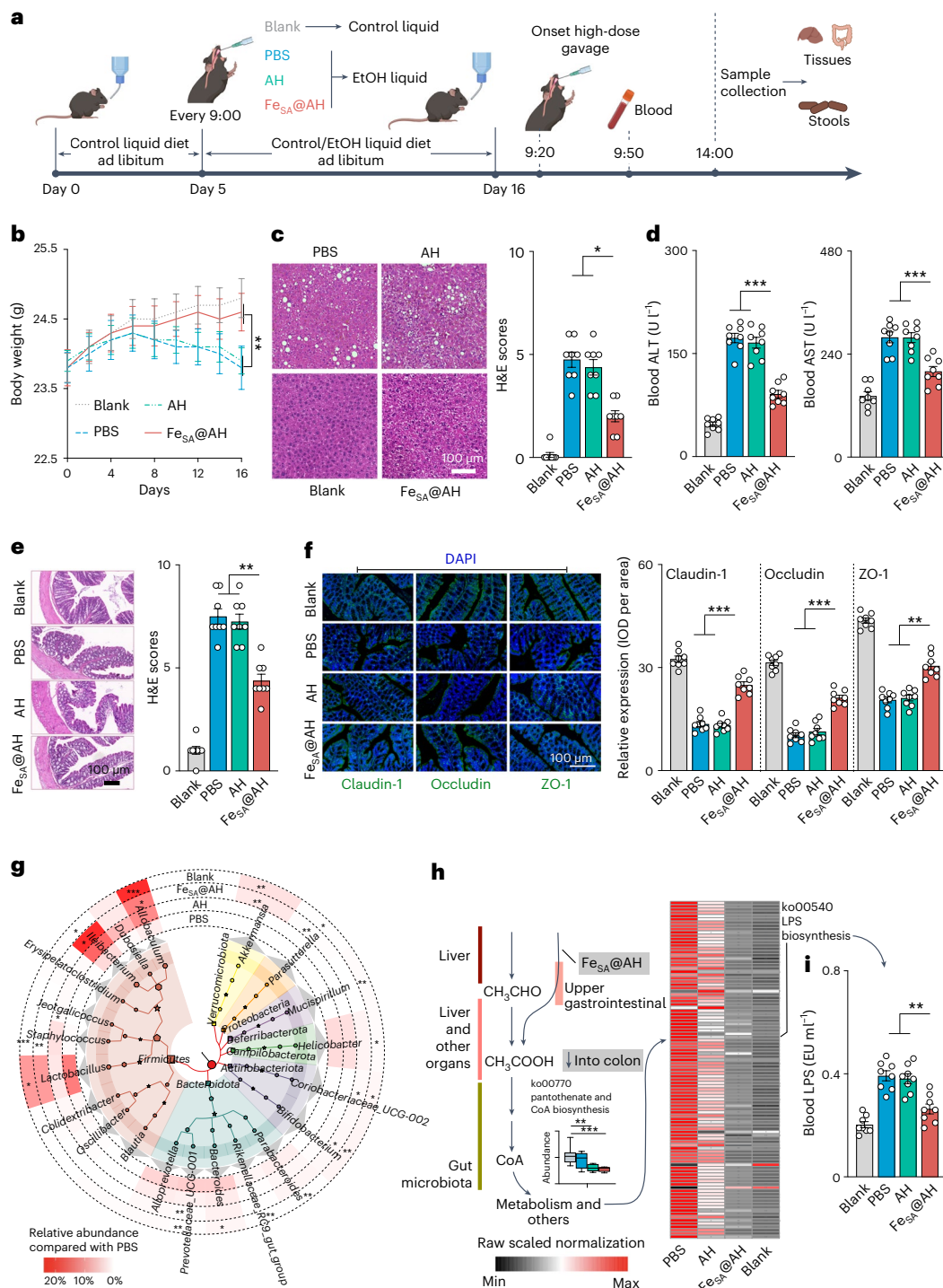
Fig. 5 | Effect of Fe_SA@AH as a prophylactic for chronic alcohol intoxication. **a**, Schematic of the chronic alcohol intoxication model construction (Methods). Created with BioRender.com. **b**, Body weight changes in the four groups of mice during the feeding period. **c**, Representative H&E-stained images of liver in the four groups. **d**, Serum ALT and AST levels in mice. **e**, H&E images of colon (left part) and its assessed scores (right histogram) in different groups of mice. **f**, Immunofluorescence staining of the tight junction proteins in the colon (left part, 30× magnification). The tight junction proteins (Claudin-1, occludin and ZO-1) were stained green whereas the 4,6-diamidino-2-phenylindole (DAPI) was blue. The histograms (right) show the mean density of the normalized levels of occludin and ZO-1. IOD, integrated optical density. **g**, Taxonomic and phylogenetic tree of the top 21 most affected genera (genus with >10% mean abundance change in at least one group compared to others) by different treatments generated by GraPhlAn 4.0. Outer circles show the grouped mean

relative abundance of each genus. **h**, Metabolic processes of alcohol to acetate and further in mice. The left colour blocks indicate the endogenous organs, liver, intestine and gut microbiota involved in alcohol decomposition, and the right shows the path in which Fe_SA@AH participated. The box-plot shows the relative levels of ko00770 pantothenate and CoA biosynthesis among groups (minimum–maximum). The heatmap shows 83 significantly changed pathways compared with those in the PBS group. Source data are provided as a Source Data file. **i**, LPS concentrations of mice in the four groups. Data are shown in the form of mean ± s.e.m. from $n = 8$ biological replicates. In **c**,**e**,**f**, the images displayed are representative of three independent biological replicates ($n = 3$), each producing consistent results. For histopathological, physiological and biochemical indexes (**c**–**f**,**i**), P values were tested by one-way analysis of variance followed by Tukey–Kramer test whereas the pairwise Wilcoxon test with Bonferroni–Holm correction was used for microbial taxa (**h**,**i**). *$P < 0.05$, **$P < 0.01$, ***$P < 0.001$.

the liver played a core role in ethanolic metabolism. Prophylactic Fe$_{SA}$@AH immediately and persistently reduced the mice blood alcohol (BA) concentration by a significant amount (Fig. 4h). The BA in Fe$_{SA}$@AH mice decreased by 41.3%, 40.4%, 42.0%, 46.6% and 55.8%, respectively, 30, 60, 120, 180 and 300 min post-gavaging. Importantly, the above-mentioned process induced no additional acetaldehyde (BAce) accumulation in blood (Fig. 4i), which plays a crucial role in safeguarding the liver, as the build-up of acetaldehyde is known to be a catalyst for liver cirrhosis and hepatocellular carcinoma. Stress responses of liver were definitely mitigated, which was revealed by the significantly decreased blood alanine aminotransferase (ALT), aspartate aminotransferase (AST), malondialdehyde (MDA) and glutathione (GSH) levels in the Fe$_{SA}$@AH group (Fig. 4j and Supplementary Fig. 26a,b).

Prophylactic effect on chronic alcohol intoxication

The NIAAA model (mouse model of chronic and binge ethanol feeding) was conducted to confirm the long-term beneficial effects of Fe$_{SA}$@AH[43]. After model constructions (Fig. 5a and Methods), the PBS mice showed a significantly decreased body weight, increased liver injury (ballooning degeneration and multifocal inflammatory cell infiltration) and hepatic lipid accumulation compared with the blank (Fig. 5b,c). Notably, Fe$_{SA}$@AH-rescued mice showed a significantly decreased loss in body weight, less liver damage and re-regulated hepatic lipid metabolism (Fig. 5b,c) from intoxication. Moreover, mice treated with Fe$_{SA}$@AH had lower BA than those with PBS and AH (Supplementary Fig. 27a). It is worth noting, however, that Fe$_{SA}$@AH also decreased the BAce concentration (Supplementary Fig. 27b), indicating its dominant competitive role in ethanol elimination to endogenous ADH. Significant lower blood ALT and AST levels further confirmed the inflammation alleviation effect of Fe$_{SA}$@AH on the liver (Fig. 5d). Additionally, administration of Fe$_{SA}$@AH also significantly suppressed triglyceride and total cholesterol accumulation in ethanol-fed mice (Supplementary Fig. 28e–j).

The gut and its symbionts (the microbiota) are important, but usually overlooked, alcohol-metabolizing organs[44–46]. Chronic alcohol consumption caused histopathological changes in the colon, destroyed epithelial cells, atrophied goblet cells and resulted in inflammatory cell infiltration (Fig. 5e), and also weakened permeability (Fig. 5f), which may cause more microbial components to enter the bloodstream[47]. Alcohol also induced significant compositional shifts (β-diversity) in the gut microbiota of mice (Supplementary Fig. 29a), but showed limited effects on the Shannon index and percentage of Gram-negative bacteria (Supplementary Fig. 29b,c). Consistently[48], the mean abundance of *Bacteroidota* increased in all alcohol-treated groups. Another dominant phylum, *Firmicutes*, decreased significantly in the PBS group compared with the blank group (Supplementary Fig. 29d). Interestingly, a significant loss of functional murine-mucoprotein-degrading bacteria, *Akkermansia* (*verrucomicrobiota*), and transitions of *Ileibacterium* and *Allobaculum* (blank) to *Bacteroides* and *Prevotellaceae_UCG-001* (PBS), were identified (Fig. 5g).

In terms of functional profiles, we found no significant intergroup gut microbial function changes due to ethanol-related processes (Supplementary Table 10). In accordance with previous research[47], gut microbiota were determined to be indirectly involved in ethanol metabolism, especially acetate-induced microbial anaerobic respiration, such as the glycolysis/gluconeogenesis (ko00010) and pentose phosphate pathway (ko00030) (Supplementary Table 10). Alcohol consumption also induced significantly overexpressed pantothenate. Moreover, CoA biosynthesis (ko00770) and the citrate cycle (TCA) (ko00020) constituted important carbon unit donors for further processes (Fig. 5h), such as lipopolysaccharide (LPS) biosynthesis (ko00540)−LPS is widely recognized as an endotoxin that can induce hepatic inflammation[49]. This epithelial

pathophysiological damage and intraluminal dysbiosis were significantly mitigated by Fe$_{SA}$@AH compared with other AHs (Fig. 5e–h). Furthermore, as one of the final beneficial outputs, the concentration of blood LPS was significantly decreased in Fe$_{SA}$@AH-treated mice (Fig. 5i).

In aggregate, we have demonstrated the design of a single-site iron-anchored amyloid hydrogel with remarkable catalytic oxidation capacity for alcohol as a highly efficient catalytic platform for in vivo alcohol metabolism. This work provides compelling evidence for the viability of a biomimetic-nanozyme-based hydrogel as an orally applied antidote for alcohol intoxication. Fe$_{SA}$@AH demonstrates exceptional preference for acetic acid production, enabling a rapid decrease in blood alcohol levels while simultaneously mitigating the risk of excessive acetaldehyde accumulation, and markedly surpasses the effectiveness of existing alcohol intoxication antidotes that rely on a combination of natural enzymes. Unlike the predominantly liver-centric human intrinsic alcohol metabolism, orally administered Fe$_{SA}$@AH directs this process towards the gastrointestinal tract, providing increased safety for the liver. In addition, despite this shift in the site of alcohol metabolism, there is no manifestation of additional adverse gastrointestinal symptoms; in fact, Fe$_{SA}$@AH shows a remarkable alleviation of intestinal damage and dysbiosis induced by alcohol consumption, further demonstrating its potential for clinical translation.

The findings from our study outline a general and efficient strategy for synthesizing a diverse group of orally applied biomimetic nanozymes, and establish the foundation for future investigations aimed at maximizing the potential of artificial enzyme design in different therapeutic applications.

Online content

Any methods, additional references, Nature Portfolio reporting summaries, source data, extended data, supplementary information, acknowledgements, peer review information; details of author contributions and competing interests; and statements of data and code availability are available at https://doi.org/10.1038/s41565-024-01657-7.

References

1. GBD 2016 Alcohol Collaborators. Alcohol use and burden for 195 countries and territories, 1990-2016: a systematic analysis for the Global Burden of Disease Study 2016. *Lancet* **392**, 1015–1035 (2018).
2. Rehm, J. et al. Global burden of disease and injury and economic cost attributable to alcohol use and alcohol-use disorders. *Lancet* **373**, 2223–2233 (2009).
3. GBD 2019 Diseases and Injuries Collaborators. Global burden of 369 diseases and injuries in 204 countries and territories, 1990–2019: a systematic analysis for the Global Burden of Disease Study 2019. *Lancet* **396**, 1204–1222 (2020).
4. GBD 2020 Alcohol Collaborators. Population-level risks of alcohol consumption by amount, geography, age, sex, and year: a systematic analysis for the Global Burden of Disease Study 2020. *Lancet* **400**, 185–235 (2022).
5. Xie, L. et al. The protective effects and mechanisms of modified Lvdou Gancao decoction on acute alcohol intoxication in mice. *J. Ethnopharmacol.* **282**, 114593 (2022).
6. Chen, X. et al. Protective effect of *Flos puerariae* extract following acute alcohol intoxication in mice. *Alcohol. Clin. Exp. Res.* **38**, 1839–1846 (2014).
7. Guo, J., Chen, Y., Yuan, F., Peng, L. & Qiu, C. Tangeretin protects mice from alcohol-induced fatty liver by activating mitophagy through the AMPK-ULK1 pathway. *J. Agric. Food Chem.* **70**, 11236–11244 (2022).
8. Liu, Y. et al. Biomimetic enzyme nanocomplexes and their use as antidotes and preventive measures for alcohol intoxication. *Nat. Nanotechnol.* **8**, 187–192 (2013).

9. Xu, D. et al. A hepatocyte-mimicking antidote for alcohol intoxication. *Adv. Mater.* **30**, e1707443 (2018).

10. Wang, H., Wan, K. & Shi, X. Recent advances in nanozyme research. *Adv. Mater.* **31**, e1805368 (2019).

11. Jiang, D. et al. Nanozyme: new horizons for responsive biomedical applications. *Chem. Soc. Rev.* **48**, 3683–3704 (2019).

12. Yu, Z., Lou, R., Pan, W., Li, N. & Tang, B. Nanoenzymes in disease diagnosis and therapy. *Chem. Commun.* **56**, 15513–15524 (2020).

13. Cao, C. et al. Biomedicine meets nanozyme catalytic chemistry. *Coord. Chem. Rev.* **491**, 215–245 (2023).

14. Peng, C., Pang, R., Li, J. & Wang, E. Current advances on the single-atom nanozyme and its bio-applications. *Adv. Mater.* **36**, e2211724 (2023).

15. Jiao, L. et al. When nanozymes meet single-atom catalysis. *Angew. Chem. Int. Ed.* **59**, 2565–2576 (2020).

16. Zhang, S. et al. Single-atom nanozymes catalytically surpassing naturally occurring enzymes as sustained stitching for brain trauma. *Nat. Commun.* **13**, 4744 (2022).

17. Sun, A., Mu, L. & Hu, X. Graphene oxide quantum dots as novel nanozymes for alcohol intoxication. *ACS Appl. Mater. Interfaces* **9**, 12241–12252 (2017).

18. Geng, X. et al. Confined cascade metabolic reprogramming nanoreactor for targeted alcohol detoxification and alcoholic liver injury management. *ACS Nano* **17**, 7443–7455 (2023).

19. Bolisetty, S. & Mezzenga, R. Amyloid–carbon hybrid membranes for universal water purification. *Nat. Nanotechnol.* **11**, 365–371 (2016).

20. Xu, D. et al. Food amyloid fibrils are safe nutrition ingredients based on in-vitro and in-vivo assessment. *Nat. Commun.* **14**, 6806 (2023).

21. Shen, Y. et al. Amyloid fibril systems reduce, stabilize and deliver bioavailable nanosized iron. *Nat. Nanotechnol.* **12**, 642–647 (2017).

22. Cao, Y. & Mezzenga, R. Design principles of food gels. *Nat. Food* **1**, 106–118 (2020).

23. Hu, B. et al. Amyloid–polyphenol hybrid nanofilaments mitigate colitis and regulate gut microbial dysbiosis. *ACS Nano* **14**, 2760–2776 (2020).

24. Peydayesh, M. et al. Amyloid–polysaccharide interfacial coacervates as therapeutic materials. *Nat. Commun.* **14**, 1848 (2023).

25. Scheffen, M. et al. A new-to-nature carboxylation module to improve natural and synthetic CO_2 fixation. *Nat. Catal.* **4**, 105–115 (2021).

26. Wang, C. et al. Atomic Fe hetero-layered coordination between g-C_3N_4 and graphene nanomeshes enhances the ORR electrocatalytic performance of zinc–air batteries. *J. Mater. Chem. A* **7**, 1451–1458 (2019).

27. Kim, S. et al. In situ XANES of an iron porphyrin irreversibly adsorbed on an electrode surface. *J. Am. Chem. Soc.* **113**, 9063–9066 (1991).

28. Shui, J. L., Karan, N. K., Balasubramanian, M., Li, S. Y. & Liu, D. J. Fe/N/C composite in Li–O_2 battery: studies of catalytic structure and activity toward oxygen evolution reaction. *J. Am. Chem. Soc.* **134**, 16654–16661 (2012).

29. Bagus, P. S. et al. Combined multiplet theory and experiment for the Fe 2p and 3p XPS of FeO and Fe_2O_3. *J. Chem. Phys.* **154**, 094709 (2021).

30. Nelson, G. W., Perry, M., He, S. M., Zechel, D. L. & Horton, J. H. Characterization of covalently bonded proteins on poly(methyl methacrylate) by X-ray photoelectron spectroscopy. *Colloids Surf. B* **78**, 61–68 (2010).

31. Vanea, E. & Simon, V. XPS study of protein adsorption onto nanocrystalline aluminosilicate microparticles. *Appl. Surf. Sci.* **257**, 2346–2352 (2011).

32. Ji, S. et al. Matching the kinetics of natural enzymes with a single-atom iron nanozyme. *Nat. Catal.* **4**, 407–417 (2021).

33. Chamarro, E., Marco, A. & Esplugas, S. Use of Fenton reagent to improve organic chemical biodegradability. *Water Res.* **35**, 1047–1051 (2001).

34. Meyerstein, D. Re-examining Fenton and Fenton-like reactions. *Nat. Rev. Chem.* **5**, 595–597 (2021).

35. Vonghia, L. et al. Acute alcohol intoxication. *Eur. J. Intern. Med.* **19**, 561–567 (2008).

36. Schweizer, T. A. et al. Neuropsychological profile of acute alcohol intoxication during ascending and descending blood alcohol concentrations. *Neuropsychopharmacology* **31**, 1301–1309 (2006).

37. Chen, J. et al. Glucose-oxidase like catalytic mechanism of noble metal nanozymes. *Nat. Commun.* **12**, 3375 (2021).

38. Comotti, M., Della|Pina, C., Falletta, E. & Rossi, M. Aerobic oxidation of glucose with gold catalyst: hydrogen peroxide as intermediate and reagent. *Adv. Synth. Catal.* **348**, 313–316 (2006).

39. Ishida, T. et al. Influence of the support and the size of gold clusters on catalytic activity for glucose oxidation. *Angew. Chem. Int. Ed.* **47**, 9265–9268 (2008).

40. Usuelli, M. et al. Polysaccharide-reinforced amyloid fibril hydrogels and aerogels. *Nanoscale* **13**, 12534–12545 (2021).

41. Dolganiuc, A. & Szabo, G. In vitro and in vivo models of acute alcohol exposure. *World J. Gastroenterol.* **15**, 1168–1177 (2009).

42. Zakhari, S. Overview: how is alcohol metabolized by the body? *Alcohol Res. Health* **29**, 245–254 (2006).

43. Bertola, A., Mathews, S., Ki, S. H., Wang, H. & Gao, B. Mouse model of chronic and binge ethanol feeding (the NIAAA model). *Nat. Protoc.* **8**, 627–637 (2013).

44. Mutlu, E. A. et al. Colonic microbiome is altered in alcoholism. *Am. J. Physiol. Gastrointest.* **302**, G966–G978 (2012).

45. Canesso MCC et al. Comparing the effects of acute alcohol consumption in germ-free and conventional mice: the role of the gut microbiota. *BMC Microbiol.* **14**, 1–10 (2014).

46. Keshavarzian, A. et al. Evidence that chronic alcohol exposure promotes intestinal oxidative stress, intestinal hyperpermeability and endotoxemia prior to development of alcoholic steatohepatitis in rats. *J. Hepatol.* **50**, 538–547 (2009).

47. Horowitz, A., Chanez-Paredes, S. D., Haest, X. & Turner, J. R. Paracellular permeability and tight junction regulation in gut health and disease. *Nat. Rev. Gastroenterol. Hepatol.* **20**, 417–432 (2023).

48. Martino, C. et al. Acetate reprograms gut microbiota during alcohol consumption. *Nat. Commun.* **13**, 4630 (2022).

49. Han, Y. H. et al. Enterically derived high-density lipoprotein restrains liver injury through the portal vein. *Science* **373**, eabe6729 (2021).

[1]Department of Health Sciences and Technology, ETH Zurich, Zurich, Switzerland. [2]Particle and Interfacial Technology Group, Faculty of Bioscience Engineering, Ghent University, Ghent, Belgium. [3]Department of Nutrition and Health, Beijing Higher Institution Engineering Research Center of Animal Products, China Agricultural University, Beijing, China. [4]Department of Chemistry and Applied Biosciences, ETH Zurich, Zurich, Switzerland. [5]Institute of Energy and Process Engineering, Department of Mechanical and Process Engineering, ETH Zurich, Zurich, Switzerland. [6]Institute of Translational Medicine, Zhejiang Shuren University, Zhejiang, China. [7]ICFO–Institut de Ciències Fotòniques, The Barcelona Institute of Science and Technology, Barcelona, Spain. [8]Department of Materials, ETH Zurich, Zurich, Switzerland. [9]These authors contributed equally: Jiaqi Su, Pengjie Wang. ✉e-mail: jiaqi.su@hest.ethz.ch; raffaele.mezzenga@hest.ethz.ch

Methods

Synthesis of catalysts

BLG (>98%) was purchased from Davisco Foods International and purified using a previously reported protocol[50]. For a detailed description of BLG fibril preparation, see ref. [51]. For the synthesis of Fe$_{SA}$@FibBLG, 100 mg lyophilized BLG fibril powder was dispersed in a mixture of 8.0 ml ethanol and 1.9 ml PEG200. The dispersion was then subjected to argon bubbling for 30 min to remove the dissolved oxygen, followed by irradiation under a xenon lamp with an ultraviolet filter (250–380 nm, 27.9 mW cm^{-2}, PLS-SXE300CUV) for 10 min to generate free radicals. Subsequently, 0.1 ml of 108.21 mg ml^{-1} Fe(NO$_3$)$_3$·9H$_2$O EDTA solution was added dropwise to the dispersion of BLG fibrils under magnetic stirring for 12 h at 25 °C. Fe$_{SA}$@BLG was prepared by the same synthesis procedure as for Fe$_{SA}$@FibBLG, except that the BLG fibril powder was replaced by an equal amount of BLG powder. For the synthesis of FeNP@FibBLG, the as-obtained Fe$_{SA}$@FibBLG dispersion was further ultraviolet-irradiated for 18 min under anaerobic conditions to reduce the iron ions. Finally, samples were collected by centrifugation at 4 °C, 11,100g for 10 min, washed by ethanol (10.0 ml × 6) and resuspended in 5.0 ml deionized water (pH 2). The powdered Fe$_{SA}$@FibBLG, Fe$_{SA}$@BLG and FeNP@FibBLG were obtained by lyophilization and stored at 4 °C.

Characterizations

The high-resolution TEM images and elemental mappings were recorded with an FEI Talos F200X microscope at accelerating voltages of 80 kV and 200 kV, respectively. AFM images were obtained using a Bruker Multimode 8 scanning probe microscope. HAADF-STEM images were captured using an FEI Titan Themis G2 microscope equipped with a probe spherical aberration corrector and operated at 300 keV. The crystalline structure and phase purity were detected by a powder diffractometer (Siemens D500 with Cu Kα radiation (λ = 1.5406 Å)). The iron loadings on catalysts were analysed by inductively coupled plasma mass spectrometry (Elan DRC-e, Perkin Elmer). The X-ray absorption structure spectra (Fe K-edge) were collected at beamline BL44B2 of the SPring-8 synchrotron (Japan), operated at 8.0 GeV with a maximum current of 250 mA. Data were collected in transmission mode using a Si(111) double-crystal monochromator. The EXAFS data were analysed using the ATHENA module implemented in IFEFFIT software (CARS). XPS measurements were performed using a multipurpose spectrometer (Sigma Probe, Thermo VG Scientific) with a monochromatic Al Kα X-ray source. EPR spectra were acquired using a Bruker X-band (9.4 GHz) EMXplus 10/12 spectrometer equipped with an Oxford Instruments ESR-910 liquid helium cryostat. All spectra were collected under ambient conditions. Solution ^{1}H NMR spectra were collected on a Bruker DRX 300 spectrometer (7.05 T; Larmor frequency, 300 MHz (^{1}H)) in deuterated water (D$_2$O) at room temperature.

MD simulations

All of the AAMD simulations were performed on a GROMACS 2018 package using a gromacs54A force field[52]. The box size of the initial model was 12 × 12 × 30 nm^3, including an SPC/E water model and 102 peptide chains (sequence, LACQCL)[19] under three-dimensional periodic boundary conditions. A spherical cut-off of 1.0 nm was used for the summation of van der Waals interactions and short-range Coulomb interactions, and the particle-mesh Ewald method[53]. The temperature and pressure of the system were controlled by means of a velocity rescaling thermal thermostat and a Berendsen barostat. At first, the energy of the system was minimized in small steps to balance the initial velocity of the molecules. Then, the NPT ensemble using a leapfrog integrator with a time step of 1.0 fs was used to simulate the system for 8 ns at 300 K, which is sufficient for the balance of the system. Dynamic snapshot images were generated in Visual Molecular Dynamics 1.9.3[54].

DFT calculations

To investigate the interaction between iron ions and the system, one iron ion was inserted into the peptide dimer, and the structure was optimized by DFT using the CP2K software package[55]. The Perdew–Burke-Ernzerhof generalized gradient approximation functional was adopted to describe the electronic exchange and correlation, in conjunction with the DZVP-MOLOPT-SR-GTH basis set for all atoms (C, H, O, N, Fe). The structure was optimized with the spin multiplicity to treat the doublet spin state and the charge of the iron ion was set to +2e. The convergence criterion for the absolute value of the maximum force was set to 4.5 × 10^{-4} a.u. and the r.m.s. of all forces to 3 × 10^{-4} a.u. Grimme's DFT-D3 method was adopted for correcting van der Waals interactions[56]. The interaction of the system was characterized by the independent gradient model method, and the based isosurface maps were rendered by Visual Molecular Dynamics from the cube files exported from Multiwfn 3.8 (ref. [57]).

Peroxidase-like activity

The peroxidase-like activities of nanozymes were assessed at 37 °C using 350 μl of HAc–NaAc buffer (0.1 M, pH 4.0) with varied nanozyme concentrations, using TMB as the substrate. Following the addition of 20 μl of TMB solution (20 mM in dimethylsulfoxide) and 20 μl of H$_2$O$_2$ solution (2 M), 10 μl of nanozymes with varying concentrations was introduced into the system. The catalytic oxidation of TMB (oxTMB) was quantified by measuring the absorbance at 652 nm via an ultraviolet–visible spectrometer. The steady-state kinetics analysis was executed by modifying the concentrations of TMB and H$_2$O$_2$. To derive the Michaelis–Menten constant, we performed Lineweaver–Burk plot analysis using the double reciprocal of the Michaelis–Menten equation, $v = v_{max} \times [S]/(K_m + [S])$, where v denotes the initial velocity, v_{max} represents the maximum reaction velocity, $[S]$ indicates the substrate concentration and K_m is the Michaelis constant. Additionally, the catalytic rate constant (k_{cat}) was computed as $k_{cat} = v_{max}/[E]$, where $[E]$ signifies the molar concentration of metal within the nanozymes. By employing diverse pH buffer solutions, we explored the pH dependency of the peroxidase-like activity of nanozymes, spanning a range from pH 2 to 9. Similarly, we investigated its temperature sensitivity by observing its activity at various temperatures, progressively increasing from 20 °C to 60 °C.

Catalytic oxidation activity on alcohol and acetaldehyde

The catalytic oxidation activities of nanozymes on both alcohol and acetaldehyde were carried out at 37 °C in 350 μl of HAc–NaAc buffer (0.1 M, pH 4.0), with varying nanozyme concentrations (10 μl). Subsequent to adding 20 μl of H$_2$O$_2$ solution (2 M), 20 μl of ethanol or acetaldehyde solution (2 mM) was introduced into separate tubes containing the reaction mixture. Quantification of the catalytic oxidation of ethanol or acetaldehyde was performed using the Ethanol Assay Kit (ab65343) and Acetaldehyde Assay Kit (ab308327) from Abcam Biotechnology. Through altering the concentrations of ethanol or acetaldehyde, steady-state kinetics analysis was carried out, and the Michaelis–Menten constant was determined by analysing Lineweaver–Burk plots involving the double reciprocal of the Michaelis–Menten equation. Additionally, the identification of the reaction products was confirmed by ^{1}H NMR spectrometry.

Catalytic activity assessment of nanozymes during in vitro simulation of the digestion process

We adhered to the INFOGEST standard protocol for nanozyme digestion to replicate the physiological human gastrointestinal digestion process[58]. In this methodology, stock solutions of simulated gastric fluid and simulated intestinal fluid were prepared and equilibrated at 37 °C prior to use. For gastric digestion, 2 ml of the nanozyme (1 mg ml^{-1}) was mixed with 2 ml of simulated gastric fluid stock solution, and porcine pepsin solution was added to achieve a final enzyme activity of 500 U per mg of protein. CaCl$_2$(H$_2$O)$_2$ was then introduced into the mixture to reach a final concentration of 0.15 mM prior to adjusting the pH to 3 using 5 M HCl. The mixture was transferred to

a water bath shaker (VWR 462-0493) at 37 °C and sampled at 30 and 60 min, after which NaOH solution was used to deactivate the enzyme. Following the gastric digestion, pancreatin (0.1 mg ml⁻¹) was dissolved in simulated intestinal fluid containing 0.6 mM $CaCl_2$ and added to the gastric digests in a 1:1 (v/v) ratio to initiate intestinal digestion, which lasted for 120 min at 37 °C with regular sampling every 30 min. The samples were freeze-dried immediately after collection for enzyme activity evaluation experiments using TMB as a substrate, in which the amount of nanozyme after digestion was normalized.

Hydrogel formation

Gelation of Fe_{SA}@FibBLG dispersion containing AuNPs (Fe_{SA}@AH) was achieved following our previously reported procedure with some modifications[40]. For the synthesis of AuNPs, all glassware was cleaned with freshly prepared aqua regia (HCl:HNO$_3$ = 3:1 vol/vol) and then thoroughly rinsed with water. A 2 ml solution of BLG fibrils (2.0 wt%, pH 2.0) was mixed with a 40 mM HAuCl$_4$ solution to reach a final protein:gold mass ratio of 14.7:1. The mixture underwent a chemical reduction through the dropwise addition of a NaBH$_4$ solution (0.8 ml) under a nitrogen atmosphere. The resulting solution was then dialysed to remove any remaining NaBH$_4$ and concentrated to 2 ml with a dialysis membrane (Spectra/Por, molecular weight cut-off, 6–8 kDa, Spectrum Laboratories) against a 6 wt% PEG solution ($M_r \approx 35,000$, Sigma-Aldrich) at pH 2.0. TEM imaging of AuNPs stabilized by BLG fibrils revealed three-dimensional particles with an average size of 1.32 nm (Supplementary Fig. 21a), determined by analysing six TEM images using ImageJ software v.1.8.0. For the preparation of Fe_{SA}@AH, 2 g of Fe_{SA}@FibBLG powder was dissolved in the resulting AuNP-attached BLG fibril solution (2 ml). The mixture was then transferred into a plastic syringe, the top part of which had been previously cut. The plastic syringe was covered with a section of a dialysis tube (Spectra/Por, molecular weight cut-off, 6–8 kDa), and the head of the syringe was positioned in direct contact with an excess of 300 mM NaCl solution at pH 7.4 for at least 16 h in a 4 °C cold room to facilitate gelation. The resulting hydrogel sample was kept under 4 °C. The working hydrogel was freshly prepared by mixing the aforementioned hydrogel with 0.1 ml of a glucose solution (8.0 M) immediately before further characterization or detoxification use. A BLG fibril hydrogel was obtained using the same procedure, except that the Fe_{SA}@FibBLG was replaced with an equal amount of BLG fibril dispersion.

Murine models

Male wild-type C57BL/6 mice, 20–25 g and 8–10 weeks old, were purchased from Beijing Vital River Laboratory Animal Technology. All of the murine experiments in the current study were approved by the Regulations of Beijing Laboratory Animal Management (approval number AW40803202-5-1) and conducted according to the guidelines set forth in the Institutional Animal Care and Use Committee of China Agricultural University.

Acute model

Thirty-two male C57BL/6 mice were randomly divided into four groups after 12 h fasting. Mice were orally gavaged with AH and Fe_{SA}@AH (at doses of 10 ml per kg (body weight)), and two groups of mice received the same volume of PBS (as controls, the blank and the PBS groups), respectively. After 20 min of adaptation, mice from the AH, Fe_{SA}@AH, and PBS groups were orally administered an alcohol liquid diet (10 g per kg (body weight)), while the same volume of PBS was administered for the blank group. All the mice were killed 6 h later.

Chronic model

A mouse model of chronic and binge ethanol feeding (NIAAA model) was conducted following the protocol proposed by Bertola et al.[43]. In brief, after 5 days of ad libitum Lieber–DeCarli diet adaptation, 32 mice were randomly divided into four groups: (1) a control group

(Con) of mice were pair-fed with the control diet; (2) an ethanol diet group (EtOH); (3) an ethanol diet group with additional 10 ml per kg (body weight) AH; and (4) an ethanol diet group with additional 10 ml per kg (body weight) Fe_{SA}@AH. The ethanol-fed groups were granted unrestricted access to the ethanol Lieber–DeCarli diet containing 5% (vol/vol) ethanol for 10 days, and additionally received daily morning (9:00) gavage of PBS, AH or Fe_{SA}@AH, respectively. The control group was pair-fed with an isocaloric control diet and daily control-liquid gavage. All animals were maintained in specific pathogen-free conditions, at a temperature of 23 ± 1 °C and 50–60% humidity, under a 12 h light/dark cycle, with access to autoclaved water. On day 16, both the ethanol-fed and pair-fed mice were orally administered a single dose of ethanol (5 g per kg (body weight)) or isocaloric maltose dextrin at 9:20, respectively, and killed 6 h later. The body weight of mice was recorded every 2 days.

MicroPET

After overnight fasting, mice were gavaged with 0.1 ml [¹⁸F]FDG-labelled Fe_{SA}@AH. Then, mice were anaesthetized with oxygen containing 2% isoflurane, and placed in and fixed in a prone position in an imaging chamber. Time-series images were obtained with an Inveon microPET/CT scanner (Siemens); the scanner parameters were a 15 min CT scan (80 kVp, 500 µA, 1,100 ms exposure time) followed by a 10 min PET acquisition. Quantification of images was performed by AMIDE software 3.0.

Alcohol tolerance test

Approximately 10 µl of blood was collected from the submandibular vein at 30, 60, 90, 120, 180 and 300 min after alcohol exposure. In the chronic model, sampling was conducted after the binge ethanol feeding. Blood alcohol concentration (BAC) was determined using a test kit from Abcam Biotechnology (ab65343). BACs were normalized to mice body weights as previously described[8]. Normalized BAC, BAC_{nor}, was calculated using the equation: $BAC_{nor} = BAC_i \times (BWT_i/BWT_{ave})$, where BAC_i and BWT_i denote the blood alcohol level and body weight of mice, respectively, and BWT_{ave} represents the average weight of all mice in each set of experiments. The quantification of the BAce concentration was carried out using a test kit obtained from Abcam Biotechnology (ab308327), and the normalization process was conducted using the same method as for the BAC.

Alcohol tolerance time was the duration between alcohol administration and the absence of righting reflex, while the duration of the absence of righting reflex was recorded as the sobering-up time. Mice that became ataxic were considered to have lost their righting reflex, and were then placed face up. The time point at which the mice returned to their normal upright position signified they had regained their righting reflex.

MWM test

An MWM test[59] was conducted by Anhui Zhenghua Biologic Apparatus Facilities, as described previously. Specifically, the MWM apparatus comprised a large circular pool (120 cm diameter and 40 cm height) which was filled with TiO_2-dyed, 25 °C thermostatic water, and a 10-cm-diameter platform was positioned and fixed 2 cm below the water surface. Before acute ethanol exposure, mice received four rounds of daily training for 6 days. Each trial was limited to 60 s, and the time that it took for the mice to successfully locate the platform was recorded. On day 7, mice were retested (no platform condition) 5 h after ethanol feeding (the time point by which all mice regained their consciousness and mobility). The tested items included trajectory, path length, escape latency and swimming speed (MWM animal behaviour video tracking system, Morris v.2.0).

Biochemical assays

Blood samples were collected through cardiac puncture from anaesthetized mice 6 h after alcohol gavage. Prior to testing, samples were

maintained at ambient temperature for 4 h, and then centrifuged (864.9g, 4 °C) for 20 min. Supernatants were suctioned and stored at −80 °C for further analysis. Serum ALT, AST, triglycerides and total cholesterol were measured by a Hitachi Biochemistry Analyzer 7120 (Hitachi High-Tech).

Weighed liver tissues were collected and immersed immediately in 10% neutral buffered formaldehyde. After overnight fixation, tissues were embedded in paraffin and cut into 5 µm sections for further haematoxylin and eosin (H&E) and oil red O (Sigma) staining. Images were captured by a Nikon Eclipse TI-SR fluorescence microscope. Fresh liver was homogenized in chilled normal saline and centrifuged (1,500g, 4 °C) for 15 min. GSH and MDA levels of the resultant supernatant were detected using the GSH assay kit (ab65322) and the lipid peroxidation (MDA) assay kit (ab118970), respectively. Hepatic and cellular lipid content was isolated using the chloroform/methanol-based method[60], and quantified by using the triglyceride assay kit (ab65336) and the mouse total cholesterol ELISA kit (ab285242, SSUF-C), respectively.

Colon histology and immunohistochemistry
Colon length, caecum to anus, was measured, and the distal colon was washed with saline, with one-half being fixed with 4% paraformaldehyde, and the other half stored at −80 °C. Histological measurements of the colon were the same as those for the liver.

For immunofluorescence, colon tissues were treated with EDTA buffer and boiled to expose the antigens. Tissues were then incubated overnight at 4 °C with primary antibody and washed three times for 5 min each with PBS. Subsequently, colon tissues were covered with secondary antibody and incubated at room temperature in the dark for 50 min, followed by another set of three 5 min washes with PBS. The resultant sections were mounted with a mounting medium and stained with 4,6-diamidino-2-phenylindole. Slides were then covered, and the images were captured using a Nikon Eclipse Ti inverted fluorescence microscope.

Microbiota changes
Faecal samples were collected within 5 min after defecation into a sterile tube and stored at −80 °C. Microbial genome DNA was extracted from faeces by using the DNeasy PowerSoil Pro Kit (QIAGEN) according to the manufacturer's instructions, and the variable 3–4 (V4-v4) region of the 16S rRNA gene was PCR-amplified using barcoded 338F-806R primers (forward primer, 5′-ACTCCTACGGGAGGCAGCAG-3′; reverse primer, 5′-GGACTACHVGGGTWTCTAAT-3′). PCR components contained 25 µl of Phusion High-Fidelity PCR Master Mix, 3 µl (10 µM) of each forward and reverse primer, 10 µl of the DNA template, 3 µl of DMSO and 6 µl of double-distilled H2O. The following cycling conditions were used: initial denaturation at 98 °C for 30 s, followed by 25 cycles of denaturation at 98 °C for 15 s, annealing at 58 °C for 15 s, and extension at 72 °C for 15 s, and a final extension of 1 min at 72 °C. PCR amplicons were purified using Agencourt AMPure XP Beads (Beckman Coulter) and quantified using a PicoGreen dsDNA Assay Kit (Invitrogen). After quantification, amplicons were pooled in equal amounts, and 2 × 150 bp paired-end sequencing was performed using the Illumina Miseq PE300 platform at GUHE Info Technology. Amplicon sequence variants (ASVs) were denoised and clustered by the UNOISE algorithm. Taxa bar plots, and α- and β-diversity analysis, were performed with QIIME 2 v.2020.6 and the R package v.3.6.3. Metabolic function was predicted using PICRUSt2, and the output file was further analysed using the STAMP software package (v.2.1.3).

Reporting summary
Further information on research design is available in the Nature Portfolio Reporting Summary linked to this article.

Data availability
All the data that validates the outcomes of this study are included in the Article and its Supplementary Information files. For any other relevant source data, interested parties can obtain them from the corresponding authors upon reasonable request. Source data are provided with this paper.

Code availability
Simulation files and code used for modelling iron-anchored BLG fibril segments can be accessed via Zenodo at: https://doi.org/10.5281/zenodo.10819612 (ref. 61).

References
50. Jung, J.-M., Savin, G., Pouzot, M., Schmit, C. & Mezzenga, R. Structure of heat-induced β-lactoglobulin aggregates and their complexes with sodium-dodecyl sulfate. *Biomacromolecules* **9**, 2477–2486 (2008).
51. Jung, J.-M. & Mezzenga, R. Liquid crystalline phase behavior of protein fibers in water: experiments versus theory. *Langmuir: ACS J. Surf. Colloids* **26**, 504–514 (2010).
52. Kutzner, C. et al. Best bang for your buck: GPU nodes for GROMACS biomolecular simulations. *J. Comput. Chem.* **36**, 1990–2008 (2015).
53. Wennberg, C. L. et al. Direct-space corrections enable fast and accurate Lorentz–Berthelot combination rule Lennard–Jones lattice summation. *J. Chem. Theory Comput.* **11**, 5737–5746 (2015).
54. Humphrey, W., Dalke, A. & Schulten, K. VMD—Visual Molecular Dynamics. *J. Mol. Graph.* **14**, 33–38 (1996).
55. Kuhne, T. D. et al. CP2K: An electronic structure and molecular dynamics software package—Quickstep: efficient and accurate electronic structure calculations. *J. Chem. Phys.* **152**, 194103 (2020).
56. Grimme, S., Antony, J., Ehrlich, S. & Krieg, H. A consistent and accurate ab initio parametrization of density functional dispersion correction (DFT-D) for the 94 elements H–Pu. *J. Chem. Phys.* **132**, 154104 (2010).
57. Lu, T. & Chen, F. Multiwfn: a multifunctional wavefunction analyzer. *J. Comput. Chem.* **33**, 580–592 (2012).
58. Brodkorb, A. et al. INFOGEST static in vitro simulation of gastrointestinal food digestion. *Nat. Protoc.* **14**, 991–1014 (2019).
59. Vorhees, C. V. & Williams, M. T. Morris water maze: procedures for assessing spatial and related forms of learning and memory. *Nat. Protoc.* **1**, 848–858 (2006).
60. Folch, J., Lees, M. & Sloane Stanley, G. H. A simple method for the isolation and purification of total lipides from animal tissues. *J. Biol. Chem.* **226**, 497–509 (1957).
61. Su, J. Code for MD and DFT. *Zenodo* https://doi.org/10.5281/zenodo.10819612 (2024).

Author contributions
R.M. and J.S. conceived the idea, designed the experiments, co-wrote the manuscript and coordinated the overall research project. J.S. developed the fabrication procedure of protein-fibril-based

Competing interests

J.S. and R.M. are the inventors of a patent filed jointly by Ghent University and ETH Zurich (EP24153321).

Additional information

Supplementary information The online version contains supplementary material available at https://doi.org/10.1038/s41565-024-01657-7.

Correspondence and requests for materials should be addressed to Jiaqi Su or Raffaele Mezzenga.

Peer review information *Nature Nanotechnology* thanks Marco Frasconi and the other, anonymous, reviewer(s) for their contribution to the peer review of this work.

Reprints and permissions information is available at www.nature.com/reprints.

natureportfolio

Corresponding author(s):   Raffaele Mezzenga

Last updated by author(s):   March 15th, 2024

Reporting Summary

Nature Portfolio wishes to improve the reproducibility of the work that we publish. This form provides structure for consistency and transparency in reporting. For further information on Nature Portfolio policies, see our Editorial Policies and the Editorial Policy Checklist.

Please do not complete any field with "not applicable" or n/a. Refer to the help text for what text to use if an item is not relevant to your study.
For final submission: please carefully check your responses for accuracy; you will not be able to make changes later.

Statistics

For all statistical analyses, confirm that the following items are present in the figure legend, table legend, main text, or Methods section.

n/a	Confirmed	
☐	☒	The exact sample size (n) for each experimental group/condition, given as a discrete number and unit of measurement
☐	☒	A statement on whether measurements were taken from distinct samples or whether the same sample was measured repeatedly
☐	☒	The statistical test(s) used AND whether they are one- or two-sided *Only common tests should be described solely by name; describe more complex techniques in the Methods section.*
☐	☒	A description of all covariates tested
☒	☐	A description of any assumptions or corrections, such as tests of normality and adjustment for multiple comparisons
☒	☐	A full description of the statistical parameters including central tendency (e.g. means) or other basic estimates (e.g. regression coefficient) AND variation (e.g. standard deviation) or associated estimates of uncertainty (e.g. confidence intervals)
☐	☒	For null hypothesis testing, the test statistic (e.g. F, t, r) with confidence intervals, effect sizes, degrees of freedom and P value noted *Give P values as exact values whenever suitable.*
☒	☐	For Bayesian analysis, information on the choice of priors and Markov chain Monte Carlo settings
☒	☐	For hierarchical and complex designs, identification of the appropriate level for tests and full reporting of outcomes
☒	☐	Estimates of effect sizes (e.g. Cohen's d, Pearson's r), indicating how they were calculated

Our web collection on statistics for biologists contains articles on many of the points above.

Software and code

Policy information about availability of computer code

Data collection	All of the all-atom MD simulations were performed on a GROMACS 2018 package. The DFT calculations were performed using the CP2K software package (version 8.1). For Intestinal flora analysis, in Taxa bar plots, and alpha- and beta-diversity analysis, were performed with the QIIME 2 (vision 2020.6) and R package (vision 3.6.3), and metabolic function was predicted using PICRUSt2. Amplicon sequence variants (ASVs) were denoised and clustered by the UNOISE algorithm.
Data analysis	For the MD simulations, dynamic snapshot images were generated in Visual Molecular Dynamics (VMD) 1.9.3. For the DFT calculations, the based isosurface maps were rendered by VMD from the cube files exported from Multiwfn 3.8. For Intestinal flora analysis, the output file of metabolic function was analyzed using the STAMP software package (version 2.1.3).

For manuscripts utilizing custom algorithms or software that are central to the research but not yet described in published literature, software must be made available to editors and reviewers. We strongly encourage code deposition in a community repository (e.g. GitHub). See the Nature Portfolio guidelines for submitting code & software for further information.

Data

Policy information about availability of data

All manuscripts must include a data availability statement. This statement should provide the following information, where applicable:
- Accession codes, unique identifiers, or web links for publicly available datasets
- A description of any restrictions on data availability
- For clinical datasets or third party data, please ensure that the statement adheres to our policy

> Source data are provided with this paper. Additional raw and analyzed datasets generated during this study are available for research purpose from the authors upon request. As R.M. and J.S. have declared a competing interest we prefer to be in a position to track those individuals using/accessing our data. Hence a data on request policy is more appropriate in this case.

Human research participants

Policy information about studies involving human research participants and Sex and Gender in Research.

Reporting on sex and gender	N/A
Population characteristics	N/A
Recruitment	N/A
Ethics oversight	N/A

Note that full information on the approval of the study protocol must also be provided in the manuscript.

Field-specific reporting

Please select the one below that is the best fit for your research. If you are not sure, read the appropriate sections before making your selection.

☒ Life sciences   ☐ Behavioural & social sciences   ☐ Ecological, evolutionary & environmental sciences

For a reference copy of the document with all sections, see nature.com/documents/nr-reporting-summary-flat.pdf

Life sciences study design

All studies must disclose on these points even when the disclosure is negative.

Sample size	No statistical methods were used to pre-determine sample sizes but our sample sizes are similar to that reported in a previous publication (Nature nanotechnology 8.3 (2013): 187-192).
Data exclusions	No sample was excluded from all analysis.
Replication	In our research, we performed experiments across at least 3 biological replicates, and findings were reproducible. Most of the experiments were replicated as stated in the figure legends. In terms of biological experiments, the reported data correspond to the main values derived from biological replicates including error. For images from microscopies, such as TEM, AFM, and so on, representative images were selected from at least six technical replicates.
Randomization	Samples and animals were randomized into different groups.
Blinding	Investigators were not blinded to group allocation.

Reporting for specific materials, systems and methods

We require information from authors about some types of materials, experimental systems and methods used in many studies. Here, indicate whether each material, system or method listed is relevant to your study. If you are not sure if a list item applies to your research, read the appropriate section before selecting a response.

Materials & experimental systems

n/a	Involved in the study
☒	Antibodies
☒	Eukaryotic cell lines
☒	Palaeontology and archaeology
☐	☒ Animals and other organisms
☒	Clinical data
☒	Dual use research of concern

Methods

n/a	Involved in the study
☒	ChIP-seq
☐	☒ Flow cytometry
☒	MRI-based neuroimaging

Animals and other research organisms

Policy information about studies involving animals; ARRIVE guidelines recommended for reporting animal research, and Sex and Gender in Research

Laboratory animals	Male, wild type (WT) C57BL/6 mice aged 8-10 weeks, were purchased from Beijing Vital River Laboratory Animal Technology Co., Ltd. All animals were housed in SPF conditions at 23±1 °C with 50-60% humidity in a 12-hour light/dark cycle and were provided autoclaved water.
Wild animals	The study did not involved wild animals.
Reporting on sex	This information has not been collected.
Field-collected samples	This study did not involve samples collected from the field.
Ethics oversight	All of the murine experiments in the current study were approved by the Regulations of Beijing Laboratory Animal Management (approval number: AW40803202-5-1) and conducted according to the guidelines set forth in the Institutional Animal Care and Use Committee of China Agricultural University.

Note that full information on the approval of the study protocol must also be provided in the manuscript.

Flow Cytometry

Plots

Confirm that:

☒ The axis labels state the marker and fluorochrome used (e.g. CD4-FITC).

☒ The axis scales are clearly visible. Include numbers along axes only for bottom left plot of group (a 'group' is an analysis of identical markers).

☒ All plots are contour plots with outliers or pseudocolor plots.

☒ A numerical value for number of cells or percentage (with statistics) is provided.

Methodology

Sample preparation	Six-well plate seeded Caco-2 cells (2 mL and 3×105 cells/well) were treated with AH or Fe1@AH after 24 h of resuscitation under the following conditions: DMEM containing 10%(v/v) fetal bovine serum (FBS), nonessential amino acids, and 1% (v/v) penicillin–streptomycin (10,000 U/mL penicillin and 10 mg/mL streptomycin) at 37 °C in 5% CO_2. The same amounts (4.0 g/mL, 40 μL) of AH or Fe1@AH were incubated with cells for another 24 h at 37 °C in 5% CO_2. Cells treated with PBS were used as a negative control. After exposure, cells were washed three times in cold PBS, centrifuged at 1500rpm for 5min, and re-suspended in 500 μL of binding buffer. The cells were then Annexin V-FITC (Invitrogen™) stained.
Instrument	The cellular fluorescence was detected using a BD FACSCalibur 2 flow cytometer.
Software	BD FACSTM software for data collection. FlowJo_v10.8.1 for data analysis.
Cell population abundance	At least 100,000 cells were measured for each sample.
Gating strategy	FSC vs. SSC gating to exclude debris. Boundaries for Gate 4 were based on the PBS-inoculated control. Bottom right quadrant, FITC 9(+)/PI(−), early apoptotic cells; top right quadrant, FITC(+)/PI(+), necrotic cells; bottom lift quadrant, FITC(−)/PI(−), viable cells.

☒ Tick this box to confirm that a figure exemplifying the gating strategy is provided in the Supplementary Information.